INTERNATIONAL JOURNAL FOR NUMERICAL METHODS IN FLUIDS, VOL. 23, 897–921 (1996)

NUMERICAL SIMULATION OF UNSTEADY VISCOUS FLOWS USING AN IMPLICIT PROJECTION METHOD

A. PENTARIS AND S. TSANGARIS

Laboratory of Aerodynamics, National Technical University of Athens, PO Box 64070, 15710 Zografou, Athens, Greece

SUMMARY

In this paper an implicit projection method for the solution of the two-dimensional, time-dependent, incompressible Navier–Stokes equations is presented. The basic principle of this method is that the evaluation of the time evolution is split into intermediate steps. The computational method is based on the approximate factorization technique. The coupled approach is used to link the equations of motion and the turbulence model equations. The standard $k-\epsilon$ turbulence model is used. The current methodology, which has been tested extensively for steady problems, is now applied for the numerical simulation of unsteady flows. Several cases were tested, such as plane or axisymmetric channels, a backward-facing step, a square cavity and an axisymmetric stenosis.

KEY WORDS: Navier–Stokes equations; unsteady flow; laminar flow; turbulent flow; projection method; approximate factorization technique

1. INTRODUCTION

The numerical prediction of unsteady incompressible flow fields has always been one of the most challenging areas of fluid dynamics. The primary difficulty is in finding a satisfactory way to link changes in the velocity fields to changes in the pressure field. This interaction must be accomplished in such a manner as to ensure that the divergence of the velocity vanishes at each level of physical time. The most common solution to this problem is the use of an artificial compressibility methodology or a projection methodology.

The projection method for the solution of the time-dependent Navier–Stokes equations was introduced independently by Chorin[1] and Temam.[2] Subsequently an explicit version of the method was presented by Fortin *et al.*[3] The projection method is an interpretation of a fractional step method as adapted to the unsteady Navier–Stokes equations.[4] The procedure of the physical time level increment is split into two steps. Following the decomposition of Chorin,[1] a tentative velocity field is first calculated by the discretized momentum equations without the pressure gradient. At the second step the velocity components at the new time level are evaluated by correcting the tentative solution in order to satisfy the incompressibility constraint.

The solution algorithm we use in the present study is the approximate factorization technique. This is an implicit algorithm which was initially developed by Beam and Warming[5] for compressible flows but has been successfully used for incompressible steady flows as well.[6,7] Regarding the mathematical model, a projection method is developed which uses a Poisson equation for the explicit pressure derivation, while the numerical algorithm involves only the momentum equations.

CCC 0271–2091/96/090897–25

Received September 1994
Revised September 1995

The standard $k-\epsilon$ model with the wall functions equations was selected for the simulation of turbulence flows because it is well-tested and widely used. It is expected that this turbulence model will sometimes perform poorly, especially in recirculation zones.

The objective of this paper is to describe a new projection method developed for collocated grids and to present predictions for several test cases where the unsteadiness is either forced or coherent.

2. GOVERNING EQUATIONS

2.1. *Momentum equations*

The full form of the momentum equations is used, where all variables are in non-dimensional form. The reference quantities are some reference velocity u_{ref}, a reference length L_{ref}, a reference density ρ_{ref} and a reference kinematic viscosity v_{ref}. The reference value for the time is then defined as $t_{\mathrm{ref}}=L_{\mathrm{ref}}/u_{\mathrm{ref}}$ and for the pressure is the product $p_{\mathrm{ref}}=\rho_{\mathrm{ref}}u_{\mathrm{ref}}^2$. The subscripts x, y, ξ and η denote derivation. The momentum equations are

$$\frac{\partial u}{\partial t}+\frac{\partial}{\partial x}\left(u^2+\frac{p}{\rho}+\tfrac{2}{3}k\right)+\frac{\partial}{\partial y}(uv)+\alpha\frac{uv}{y}=\frac{1}{Re}\left(\frac{\partial\tau_{xx}}{\partial x}+\frac{\partial\tau_{xy}}{\partial y}+\alpha\frac{\tau_{xy}}{y}\right), \tag{1}$$

$$\frac{\partial v}{\partial t}+\frac{\partial}{\partial x}(uv)+\frac{\partial}{\partial y}\left(v^2+\frac{p}{\rho}+\tfrac{2}{3}k\right)+\alpha\frac{v^2}{y}=\frac{1}{Re}\left(\frac{\partial\tau_{xy}}{\partial x}+\frac{\partial\tau_{yy}}{\partial y}+\alpha\frac{\tau_{yy}-\tau_{\phi\phi}}{y}\right), \tag{2}$$

where $\alpha=0$ for the two-dimensional equations, $\alpha=1$ for the axisymmetric equations, $Re=u_{\mathrm{ref}}L_{\mathrm{ref}}/v_{\mathrm{ref}}$ is the Reynolds number and k is the kinetic energy, which is taken into account only if a turbulent flow is going to be simulated. Finally the stresses are

$$\tau_{xx}=2v_{\mathrm{eff}}u_x,\qquad \tau_{yy}=2v_{\mathrm{eff}}v_y,\qquad \tau_{xy}=v_{\mathrm{eff}}(u_y+v_x),\qquad \tau_{\phi\phi}=2v_{\mathrm{eff}}\frac{v}{y},$$

where v_{eff} is the effective viscosity.

2.2. *Turbulence model equations*

Turbulent flows have been successfully computed over a wide range of flow regimes with Reynolds-averaged Navier–Stokes equations using the high-Reynolds-number form[8] of the $k-\epsilon$ model. This formulation requires the use of wall functions to bridge the viscous and boundary layers in proximity to the solid wall. This approach is strictly valid only for attached shear layers and may perform poorly in recirculation zones. Experimental observations showed that the general behaviour of the boundary layer and the structure of the turbulence are not fundamentally affected by the unsteadiness of the flow.[9–11] From these observations it is well-founded to suppose that turbulence models that are used to predict steady flows are still valid for unsteady flows as well.

The non-dimensional equations of the standard $k-\epsilon$ model are the kinetic energy (k) equation

$$\frac{\partial k}{\partial t}+\frac{\partial uk}{\partial x}+\frac{\partial vk}{\partial y}+\alpha\frac{vk}{y}=\frac{1}{Re}\left[\frac{\partial}{\partial x}\left(\Gamma_k\frac{\partial k}{\partial x}\right)+\frac{\partial}{\partial y}\left(\Gamma_k\frac{\partial k}{\partial y}\right)+\frac{\alpha}{y}\left(\Gamma_k\frac{\partial k}{\partial y}\right)+\tilde{G}-Re\epsilon\right] \tag{3}$$

and the dissipation rate (ϵ) equation

$$\frac{\partial\epsilon}{\partial t}+\frac{\partial u\epsilon}{\partial x}+\frac{\partial v\epsilon}{\partial y}+\alpha\frac{v\epsilon}{y}=\frac{1}{Re}\left[\frac{\partial}{\partial x}\left(\Gamma_\epsilon\frac{\partial\epsilon}{\partial x}\right)+\frac{\partial}{\partial y}\left(\Gamma_\epsilon\frac{\partial\epsilon}{\partial y}\right)+\frac{\alpha}{y}\left(\Gamma_\epsilon\frac{\partial\epsilon}{\partial y}\right)+C_1\frac{\epsilon}{k}\tilde{G}-ReC_2\frac{\epsilon^2}{k}\right], \tag{4}$$

where the reference quantity for the kinetic energy is u_{ref}^2 and for the dissipation $u_{\text{ref}}^3/L_{\text{ref}}$. In (3) and (4), $\tilde{G}$ is the kinetic energy production term,

$$\tilde{G} = \nu_t\left[2\left(u_x^2 + v_y^2 + \alpha\frac{v^2}{y^2}\right) + (u_y + v_x)^2\right],$$

and

$$\Gamma_k = \frac{\nu_{\text{eff}}}{\sigma_k}, \qquad \Gamma_\epsilon = \frac{\nu_{\text{eff}}}{\sigma_\epsilon}, \qquad \nu_{\text{eff}} = \nu_l + \nu_t,$$

where ν_{eff} and ν_l are the effective and the kinematic viscosity respectively and ν_t is the turbulent viscosity, which is given by the relation

$$\nu_t = ReC_\mu\frac{k^2}{\epsilon}.$$

Finally the constants are

$$C_1 = 1{\cdot}44, \quad C_2 = 1{\cdot}92, \quad C_\mu = 0{\cdot}09, \quad \sigma_k = 1{\cdot}0, \quad \sigma_\epsilon = 1{\cdot}3.$$

For the above model the concept of wall functions has been employed.[8] According to this, the parallel-to-the-wall velocity U_P at the first grid point P from the wall is

$$\text{laminar sublayer}: \quad U_P = u^*y^+ \quad \text{for } y^+ \leqslant 11{\cdot}63,$$

$$\text{turbulent sublayer}: \quad U_P = \frac{u^*}{\kappa}\ln(Ey^+) \quad \text{for } y^+ > 11{\cdot}63,$$

where

$$y^+ = \frac{y}{\nu}u^*$$

is the dimensionless distance of the point P from the wall,

$$u^* = \left(\frac{\tau_w}{\rho}\right)^{1/2}$$

is the friction velocity, τ_w is the wall shear stress, y is the normal distance from the point P to the wall, $\kappa = 0{\cdot}4187$ is the von Karman constant and $E = 9{\cdot}793$ is a roughness parameter.

From the above relations and according to the position of the first point P (laminar or turbulent sublayer), it is possible to calculate the shear stress τ_w.

Finally, supposing that the shear stress is constant in the sublayer, the kinetic energy k_P and dissipation ϵ_P at the point P are found to be[8]

$$k_P = C_\mu^{-1/2}u^{*2}, \qquad \epsilon_P = C_\mu^{3/4}\frac{k_P^{3/2}}{\kappa y}. \tag{5}$$

2.3. *Transformed form of equations*

Using the system of equations (1)–(4) and performing a generalized co-ordinate transformation from the physical (x, y, t) to the computational (ξ, η, τ) domain, the following non-dimensional form of the equations is obtained:[12]

$$\partial_\tau\mathbf{Q}^n + \partial_\xi\mathbf{F}^n + \partial_\eta\mathbf{G}^n + \alpha\mathbf{E}^n + \mathbf{K}^n = \partial_\xi\mathbf{V}^n + \partial_\eta\mathbf{W}^n + \alpha\mathbf{C}^n + \mathbf{D}^n, \tag{6}$$

where the superscript n denotes the time instant. In (6), $\mathbf{Q}$ is the vector of conservative variables,

$$\mathbf{Q} = J^{-1}[u, v, k, \epsilon]^{\mathrm{T}},$$

$\mathbf{F}$, $\mathbf{G}$ and $\mathbf{E}$ are the convective fluxes,

$$\mathbf{F} = J^{-1}[uU + \tfrac{2}{3}\xi_x k, vU + \tfrac{2}{3}\xi_y k, kU, \epsilon U]^{\mathrm{T}},$$

$$\mathbf{G} = J^{-1}[uV + \tfrac{2}{3}\eta_x k, vV + \tfrac{2}{3}\eta_y k, kV, \epsilon V]^{\mathrm{T}},$$

$$\mathbf{E} = v(Jy)^{-1}[u, v, k, \epsilon]^{\mathrm{T}},$$

$\mathbf{V}$, $\mathbf{W}$ and $\mathbf{C}$ are the viscous terms,

$$\mathbf{V} = (JRe)^{-1}[\xi_x\tau_{xx} + \xi_y\tau_{xy}, \xi_x\tau_{xy} + \xi_y\tau_{yy}, \Gamma_k(\xi_x k_x + \xi_y k_y), \Gamma_\epsilon(\xi_x\epsilon_x + \xi_y\epsilon_y)]^{\mathrm{T}},$$

$$\mathbf{W} = (JRe)^{-1}[\eta_x\tau_{xx} + \eta_y\tau_{xy}, \eta_x\tau_{xy} + \eta_y\tau_{yy}, \Gamma_k(\eta_x k_x + \eta_y k_y), \Gamma_\epsilon(\eta_x\epsilon_x + \eta_y\epsilon_y)]^{\mathrm{T}},$$

$$\mathbf{C} = (JyRe)^{-1}\left[\tau_{xy}, \tau_{yy} - \tau_{\phi\phi}, \Gamma_k k_y + 2v_{\mathrm{t}}\frac{v^2}{y}, \Gamma_\epsilon\epsilon_y + 2v_{\mathrm{t}}C_1\frac{\epsilon}{k}\frac{v^2}{y}\right]^{\mathrm{T}},$$

$\mathbf{D}$ is a vector that contains terms of the $k - \epsilon$ equations,

$$\mathbf{D} = (JRe)^{-1}\left[0, 0, v_{\mathrm{t}}G' - Re\epsilon, v_{\mathrm{t}}C_1\frac{\epsilon}{k}G' - ReC_2\frac{\epsilon^2}{k}\right]^{\mathrm{T}},$$

and finally

$$\mathbf{K} = \left[\partial_\xi\left(\xi_x\frac{p}{J\rho}\right) + \partial_\eta\left(\eta_x\frac{p}{J\rho}\right), \partial_\xi\left(\xi_y\frac{p}{J\rho}\right) + \partial_\eta\left(\eta_y\frac{p}{J\rho}\right), 0, 0\right]^{\mathrm{T}} = J^{-1}\left[\frac{\partial}{\partial_x}\left(\frac{p}{\rho}\right), \frac{\partial}{\partial_y}\left(\frac{p}{\rho}\right), 0, 0\right]^{\mathrm{T}}$$

is a matrix that contains the pressure derivatives of the momentum equations.

As can be seen, the vector $\mathbf{D}$ contains in addition the axisymmetric terms of the production term $\tilde{G}$, which now takes the form

$$G' = 2(\xi_x u_\xi + \eta_x u_\eta)^2 + 2(\xi_y v_\xi + \eta_y v_\eta)^2 + (\xi_x v_\xi + \eta_x v_\eta + \xi_y u_\xi + \eta_y u_\eta)^2.$$

In the expressions above, ξ and η are the curvilinear co-ordinates connected to the Cartesian ones x and y through the generalized coordinates transformation

$$\xi = \xi(x, y, t), \qquad \eta = \eta(x, y, t), \qquad \tau = t$$

and $J = \xi_x\eta_y - \xi_y\eta_x$ is the Jacobian of the transformation. Finally, U and V are the contravariant velocities along the directions ξ and η respectively, given by the relations

$$U = \xi_t + \xi_x u + \xi_y v, \qquad V = \eta_t + \eta_x u + \eta_y v.$$

3. NUMERICAL ALGORITHM AND METHOD OF APPLICATION

3.1. Time-marching scheme

For the solution of the system of equations (6) the implicit, factored, finite difference scheme of Beam and Warming[5] is used. The temporal derivative in (6) is approximated via a generalized time differencing:

$$\begin{aligned}\mathbf{Q}^n_\tau &= \frac{1}{\Delta\tau}\frac{(1+\zeta)\Delta-\zeta\nabla}{1+\theta\Delta}\mathbf{Q}^n + O[(\theta-\tfrac{1}{2}-\zeta)\Delta\tau+\Delta\tau^2] \quad\Leftrightarrow\\ \frac{\Delta\mathbf{Q}^n}{\Delta\tau} &= \frac{\theta}{1+\zeta}\partial_\tau\mathbf{Q}^{n+1} + \frac{1-\theta}{1+\zeta}\partial_\tau\mathbf{Q}^n + \frac{\zeta}{1+\zeta}\frac{\Delta\mathbf{Q}^{n-1}}{\Delta\tau} + O[(\theta-\tfrac{1}{2}-\zeta)\Delta\tau+\Delta\tau^2],\end{aligned} \tag{7}$$

where $\Delta\mathbf{Q}^n = \mathbf{Q}^{n+1}-\mathbf{Q}^n$ and Δ and ∇ are the forward and backward differencing operators respectively. According to the choice of values of θ and ζ in (7), a first- or second-order time-accurate scheme can be derived.

After substituting (6) into (7) and preforming calculations, the following relation is derived:

$$\begin{aligned}\frac{\mathbf{Q}^{n+1}-\mathbf{Q}^n}{\Delta\tau} &= \frac{\theta}{1+\zeta}(\partial_\xi\mathbf{V}+\partial_\eta\mathbf{W}+\alpha\mathbf{C}+\mathbf{D}-\partial_\xi\mathbf{F}-\partial_\eta\mathbf{G}-\alpha\mathbf{E})^{n+1}\\ &\quad+\frac{1-\theta}{1+\zeta}(\partial_\xi\mathbf{V}+\partial_\eta\mathbf{W}+\alpha\mathbf{C}+\mathbf{D}-\partial_\xi\mathbf{F}-\partial_\eta\mathbf{G}-\alpha\mathbf{E})^n\\ &\quad-\frac{\theta}{1+\zeta}\mathbf{K}^{n+1}-\frac{1-\theta}{1+\zeta}\mathbf{K}^n\\ &\quad+\frac{\zeta}{1+\zeta}\frac{\Delta\mathbf{Q}^{n-1}}{\Delta\tau}+O[(\theta-\tfrac{1}{2}-\zeta)\Delta\tau+\Delta\tau^2].\end{aligned}$$

Using a fractional step method similar to that described by Anderson and Kristoffersen,[13] the above relation is split into two parts

$$\begin{aligned}\frac{\mathbf{Q}^*-\mathbf{Q}^n}{\Delta\tau} &= \frac{\theta}{1+\zeta}(\partial_\xi\mathbf{V}+\partial_\eta\mathbf{W}+\alpha\mathbf{C}+\mathbf{D}-\partial_\xi\mathbf{F}-\partial_\eta\mathbf{G}-\alpha\mathbf{E})^*\\ &\quad+\frac{1-\theta}{1+\zeta}(\partial_\xi\mathbf{V}+\partial_\eta\mathbf{W}+\alpha\mathbf{C}+\mathbf{D}-\partial_\xi\mathbf{F}-\partial_\eta\mathbf{G}-\alpha\mathbf{E})^n\\ &\quad+\frac{\zeta}{1+\zeta}\frac{\Delta\mathbf{Q}^{n-1}}{\Delta\tau}+O[(\theta-\tfrac{1}{2}-\zeta)\Delta\tau+\Delta\tau^2]\end{aligned} \tag{8}$$

and

$$\begin{aligned}\frac{\mathbf{Q}^{n+1}-\mathbf{Q}^*}{\Delta\tau} &= -\frac{\theta}{1+\zeta}\mathbf{K}^{n+1}-\frac{1-\theta}{1+\zeta}\mathbf{K}^n+\frac{\theta}{1+\zeta}(\partial_\xi\mathbf{V}+\partial_\eta\mathbf{W}+\alpha\mathbf{C}+\mathbf{D}-\partial_\xi\mathbf{F}-\partial_\eta\mathbf{G}-\alpha\mathbf{E})^{n+1}\\ &\quad-\frac{\theta}{1+\zeta}(\partial_\xi\mathbf{V}+\partial_\eta\mathbf{W}+\alpha\mathbf{C}+\mathbf{D}-\partial_\xi\mathbf{F}-\partial_\eta\mathbf{G}-\alpha\mathbf{E})^*,\end{aligned}$$

where $\mathbf{Q}^* = [u^*, v^*, k^*, \epsilon^*]^{\mathrm{T}}$ is a tentative flow field and $\mathbf{K}^{n+1} = \mathbf{K}^*$. Equation (8) is actually the same as (7), except that it contains equation (6) without the pressure gradients and now $\Delta\mathbf{Q}^n = \mathbf{Q}^*-\mathbf{Q}^n$. Using equation (6) and performing some simple calculations, the last of the above relations becomes

$$\begin{aligned}\frac{\mathbf{Q}^{n+1}-\mathbf{Q}^*}{\Delta\tau} &= -\frac{\theta}{1+\zeta}\mathbf{K}^{n+1}-\frac{1-\theta}{1+\zeta}\mathbf{K}^n+\frac{\theta}{1+\zeta}\partial_\tau\mathbf{Q}^{n+1}-\frac{\theta}{1+\zeta}\partial_\tau\mathbf{Q}^* \quad\Rightarrow\\ \frac{\mathbf{Q}^{n+1}-\mathbf{Q}^*}{\Delta\tau} &= -\frac{\theta}{1+\zeta-\theta}\mathbf{K}^{n+1}-\frac{1-\theta}{1+\zeta-\theta}\mathbf{K}^n.\end{aligned} \tag{9}$$

In order to satisfy the constraint $1+\zeta-\theta \neq 0$, we use the implicit, second-order time-accurate, three-point backward scheme[5] with $\theta = 1$ and $\zeta = 0{\cdot}5$.

A non-linear expression occurs for the time increment of the vector of conservative variables $\Delta\mathbf{Q}^n$.[12,14]. In order to derive a linear algebraic system of equations, a linearization of the viscous and inviscid fluxes must be performed. The inviscid fluxes, which are functions of **Q**, are linearized using a Taylor series expansion:

$$\Delta\mathbf{F}^n = \mathbf{A}^n\Delta\mathbf{Q}^n + O(\Delta\tau^2), \qquad \Delta\mathbf{G}^n = \mathbf{B}^n\Delta\mathbf{Q}^n + O(\Delta\tau^2),$$

where $\mathbf{A}^n = \partial\mathbf{F}^n/\partial\mathbf{Q}^n$ and $\mathbf{B}^n = \partial\mathbf{G}^n/\partial\mathbf{Q}^n$ are the Jacobian matrices of the vectors $\mathbf{F}^n$ and $\mathbf{G}^n$ respectively, given by

$$\mathbf{A}^n, \mathbf{B}^n = \begin{vmatrix} \alpha_t + 2\alpha_x u + \alpha_y v & \alpha_y u & \frac{2}{3}\alpha_x & 0 \\ \alpha_x v & \alpha_t + \alpha_x u + 2\alpha_y v & \frac{2}{3}\alpha_y & 0 \\ k\alpha_x & k\alpha_y & \alpha_t + \alpha_x u + \alpha_y v & 0 \\ \epsilon\alpha_x & \epsilon\alpha_y & 0 & \alpha_t + \alpha_x u + \alpha_y v \end{vmatrix},$$

where $\alpha = \xi$ for $\mathbf{A}^n$ and $\alpha = \eta$ for $\mathbf{B}^n$.

The above linearization of the inviscid fluxes ensures the second-order time accuracy of the scheme. In order that this accuracy is retained in the corresponding linearization of the viscous fluxes, it must be taken into account that the latter are all functions of $\mathbf{Q}$, $\mathbf{Q}_\xi$ and $\mathbf{Q}_\eta$. Then the viscous fluxes $\mathbf{V}^n$, $\mathbf{W}^n$ and $\mathbf{C}^n$ are first split into two parts, one of which is a function of $\mathbf{Q}$ and $\mathbf{Q}_\xi$ and the other a function of $\mathbf{Q}$ and $\mathbf{Q}_\eta$:

$$\mathbf{V}^n(\mathbf{Q}, \mathbf{Q}_\xi, \mathbf{Q}_\eta) = \mathbf{V}_1^n(\mathbf{Q}, \mathbf{Q}_\xi) + \mathbf{V}_2^n(\mathbf{Q}, \mathbf{Q}_\eta), \qquad \mathbf{W}^n(\mathbf{Q}, \mathbf{Q}_\xi, \mathbf{Q}_\eta) = \mathbf{W}_1^n(\mathbf{Q}, \mathbf{Q}_\xi) + \mathbf{W}_2^n(\mathbf{Q}, \mathbf{Q}_\eta),$$
$$\mathbf{C}^n(\mathbf{Q}, \mathbf{Q}_\xi, \mathbf{Q}_\eta) = \mathbf{C}_1^n(\mathbf{Q}, \mathbf{Q}_\xi) + \mathbf{C}_2^n(\mathbf{Q}, \mathbf{Q}_\eta) + \mathbf{C}_3^n(\mathbf{Q}),$$

where

$$\mathbf{C}_3^n = v(JRey^2)^{-1}\left[O, -2v_{\mathrm{eff}}, 2v_{\mathrm{t}}v, 2v_{\mathrm{t}}C_1\frac{\epsilon}{k}v\right]^{\mathrm{T}}.$$

The vectors $\mathbf{V}_1^n$ and $\mathbf{W}_2^n$ are linearized implicitly using a Taylor series expansion:

$$\Delta\mathbf{V}_1^n = (\mathbf{P}^n - \mathbf{R}_\xi^n)\Delta\mathbf{Q}^n + \partial_\xi(\mathbf{R}\Delta\mathbf{Q})^n + O(\Delta\tau^2),$$
$$\Delta\mathbf{W}_2^n = (\mathbf{Y}^n - \mathbf{S}_\eta^n)\Delta\mathbf{Q}^n + \partial_\eta(\mathbf{S}\Delta\mathbf{Q})^n + O(\Delta\tau^2),$$

where $\mathbf{P}^n = \partial\mathbf{V}_1^n/\partial\mathbf{Q}^n$, $\mathbf{R}^n = \partial\mathbf{V}_1^n/\partial\mathbf{Q}_\xi^n$, $\mathbf{R}_\xi^n = (\mathbf{R}^n)_\xi$, $\mathbf{Y}^n = \partial\mathbf{W}_2^n/\partial\mathbf{Q}^n$, $\mathbf{S}^n = \partial\mathbf{W}_2^n/\partial\mathbf{Q}_\eta^n$ and $\mathbf{S}_\eta^n = (\mathbf{S}^n)_\eta$. The vectors $\mathbf{V}_2^n$ and $\mathbf{W}_1^n$ are linearized explicitly:

$$\Delta\mathbf{V}_2^n = \Delta\mathbf{V}_2^{n-1} + O(\Delta\tau^2), \qquad \Delta\mathbf{W}_1^n = \Delta\mathbf{W}_1^{n-1} + O(\Delta\tau^2).$$

The Jacobian matrices are

$$\mathbf{R}^n, \mathbf{S}^n = \frac{1}{Re}\begin{vmatrix} \nu_{\text{eff}}(2\alpha_x^2 + \alpha_y^2) & \nu_{\text{eff}}\alpha_x\alpha_y & 0 & 0 \\ \nu_{\text{eff}}\alpha_x\alpha_y & \nu_{\text{eff}}(\alpha_x^2 + 2\alpha_y^2) & 0 & 0 \\ 0 & 0 & \Gamma_k(\alpha_x^2 + \alpha_y^2) & 0 \\ 0 & 0 & 0 & \Gamma_\epsilon(\alpha_x^2 + \alpha_y^2) \end{vmatrix},$$

$$(-\mathbf{P} + \mathbf{R}_\xi)^n, (-\mathbf{Y} + \mathbf{S}_\eta)^n$$

$$= \frac{J}{Re}\begin{vmatrix} \partial_\alpha\left(\frac{\nu_{\text{eff}}(2\alpha_x^2 + \alpha_y^2)}{J}\right) & \partial_\alpha\left(\frac{\nu_{\text{eff}}\alpha_x\alpha_y}{J}\right) & 0 & \\ \partial_\alpha\left(\frac{\nu_{\text{eff}}\alpha_x\alpha_y}{J}\right) & \partial_\alpha\left(\frac{\nu_{\text{eff}}(\alpha_x^2 + 2\alpha_y^2)}{J}\right) & 0 & 0 \\ 0 & 0 & \partial_\alpha\left(\frac{\Gamma_k(\alpha_x^2 + \alpha_y^2)}{J}\right) & 0 \\ 0 & 0 & 0 & \partial_\alpha\left(\frac{\Gamma_\epsilon(\alpha_x^2 + \alpha_y^2)}{J}\right) \end{vmatrix},$$

where $\alpha = \xi$ for $\mathbf{R}^n$ and $(-\mathbf{P} + \mathbf{R}_\xi)^n$ and $\alpha = \eta$ for $\mathbf{S}^n$ and $(-\mathbf{Y} + \mathbf{S}_\eta)^n$.

The fluxes $\mathbf{C}_1^n$, $\mathbf{C}_2^n$ and $\mathbf{C}_3^n$ are linearized in the same way as the inviscid fluxes and the Jacobian matrices $\mathbf{N}_1^n = \partial\mathbf{C}_1^n/\partial\mathbf{Q}^n$, $\mathbf{N}_2^n = \partial\mathbf{C}_2^n/\partial\mathbf{Q}^n$ and $\mathbf{N}_3^n = \partial\mathbf{C}_3^n/\partial\mathbf{Q}^n$ are

$$\mathbf{N}_1^n, \mathbf{N}_2^n = \frac{J_\alpha}{JRey}\begin{vmatrix} \nu_{\text{eff}}\alpha_y & \nu_{\text{eff}}\alpha_x & 0 & 0 \\ 0 & 2\nu_{\text{eff}}\alpha_y & 0 & 0 \\ 0 & 0 & \alpha_y\Gamma_k & 0 \\ 0 & 0 & 0 & \alpha_y\Gamma_\epsilon \end{vmatrix}, \qquad \mathbf{N}_3^n = \frac{2}{y^2}\begin{vmatrix} 0 & 0 & 0 & 0 \\ 0 & -\frac{\nu_{\text{eff}}}{Re} & 0 & 0 \\ 0 & 0 & 2C_\mu v^2\frac{k}{\epsilon} & -C_\mu v^2\frac{k^2}{\epsilon^2} \\ 0 & 0 & C_\mu C_1 v^2 & 0 \end{vmatrix},$$

where $\alpha = \xi$ for $\mathbf{N}_1^n$ and $\alpha = \eta$ for $\mathbf{N}_2^n$.

The same linearization is used for the fluxes $\mathbf{E}^n$ and $\mathbf{D}^n$ and the Jacobian matrices $\mathbf{T}^n = \partial\mathbf{E}^n/\partial\mathbf{Q}^n$ and $\mathbf{H}^n = \partial\mathbf{D}^n/\partial\mathbf{Q}^n$ are

$$\mathbf{T}^n = \frac{1}{y}\begin{vmatrix} v & u & 0 & 0 \\ 0 & 2v & 0 & 0 \\ 0 & k & v & 0 \\ 0 & \epsilon & 0 & v \end{vmatrix}, \qquad \mathbf{H}^n = \begin{vmatrix} 0 & 0 & 0 & 0 \\ 0 & 0 & 0 & \\ 0 & 0 & 2C_\mu\frac{k}{\epsilon}G' & -C_\mu\frac{k^2}{\epsilon^2}G' - 1 \\ 0 & 0 & C_\mu C_1 G' + C_2\frac{\epsilon^2}{k^2} & -2C_2\frac{\epsilon}{k} \end{vmatrix},$$

where the production term G' is considered to be constant.

The substitution of the linear expressions of the flux vectors into the original non-linear equation for $\Delta \mathbf{Q}^n$ leads to a strongly coupled system of equations in both spatial directions. This coupled system is solved by the approximate factorization technique,[5,14] which leads to the following two tridiagonal systems, one for each of the two directions ξ and η:

$$\left(\mathbf{I} + \frac{\theta \Delta\tau}{1+\zeta}[\partial_\xi(\mathbf{A} - \mathbf{P} + \mathbf{R}_\xi) - \partial_{\xi\xi}\mathbf{R} - \alpha \mathbf{N}_1 + \Theta_\mathrm{a}\mathbf{H}]^n\right)\cdot\Delta\tilde{\mathbf{Q}}^n = \mathrm{RHS}, \tag{10a}$$

$$\left(\mathbf{I} + \frac{\theta \Delta\tau}{1+\zeta}[\partial_\eta(\mathbf{B} - \mathbf{Y} + \mathbf{S}_\eta) - \partial_{\eta\eta}\mathbf{S} - \alpha(\mathbf{N}_2 + \mathbf{N}_3 - \mathbf{T}) + \Theta_\mathrm{b}\mathbf{H}]^n\right)\cdot\Delta\mathbf{Q}^n = \Delta\tilde{\mathbf{Q}}^n, \tag{10b}$$

where

$$\mathbf{Q}^* = \mathbf{Q}^n + \Delta\mathbf{Q}^n \quad \Leftrightarrow \quad \bar{\mathbf{Q}}^* = \bar{\mathbf{Q}}^n + J\Delta\mathbf{Q}^n, \tag{10c}$$

$$\begin{aligned} \mathrm{RHS} = {} & \frac{\Delta\tau}{1+\zeta}[\partial_\xi(-\mathbf{F} + \mathbf{V})^n + \partial_\eta(-\mathbf{G} + \mathbf{W})^n + \alpha(\mathbf{C} - \mathbf{E})^n + \mathbf{D}^n] + \frac{\theta\Delta\tau}{1+\zeta}(\partial_\xi \Delta\mathbf{V}_2^{n-1} + \partial_\eta \Delta\mathbf{W}_1^{n-1}) \\ & + \frac{\zeta}{1+\zeta}\Delta\mathbf{Q}^{n-1} + \mathbf{D}_\mathrm{e} + O\left[\left(\theta - \tfrac{1}{2} - \zeta\right)\Delta\tau_2 + \Delta\tau^2\right], \end{aligned} \tag{11}$$

$\bar{\mathbf{Q}} = J\mathbf{Q}$ is the vector of conservative variables in the physical domain, $\mathbf{D}_\mathrm{e}$ represents the artificial dissipation terms[14] and Θ_a and Θ_b are weighting functions[15] used to add the Jacobian matrix $\mathbf{H}$ in the two sweeps:

$$\Theta_\mathrm{a} = \frac{|V|}{(U^2 + V^2)^{1/2}}, \qquad \Theta_\mathrm{b} = \frac{|U|}{(U^2 + V^2)^{1/2}}.$$

3.2. Poisson equation

Equation (9) leads to the relations

$$\begin{aligned} \mathbf{Q}^{n+1} &= \mathbf{Q}^* - \Delta\tau \frac{\theta}{1+\zeta-\theta}\mathbf{K}^{n+1} - \Delta\tau\frac{1-\theta}{1+\zeta-\theta}\mathbf{K}^n, \\ u^{n+1} &= u^* - \Delta\tau\frac{\theta}{1+\zeta-\theta}\frac{\partial}{\partial_x}\left(\frac{p}{\rho}\right)^{n+1} - \Delta\tau\frac{1-\theta}{1+\zeta-\theta}\frac{\partial}{\partial_x}\left(\frac{p}{\rho}\right)^n, \\ v^{n+1} &= v^* - \Delta\tau\frac{\theta}{1+\zeta-\theta}\frac{\partial}{\partial_y}\left(\frac{p}{\rho}\right)^{n+1} - \Delta\tau\frac{1-\theta}{1+\zeta-\theta}\frac{\partial}{\partial_y}\left(\frac{p}{\rho}\right)^n, \\ & k^{n+1} = k^*, \ \epsilon^{n+1} = \epsilon^* \end{aligned} \tag{12}$$

Assuming that the continuity equation is satisfied at the time instant $n+1$,

$$\frac{\partial u^{n+1}}{\partial x} + \frac{\partial v^{n+1}}{\partial y} + \alpha\frac{v^{n+1}}{y} = 0,$$

the first two equations (12) are combined to give the Poisson equation (with $P = p/\rho$)

$$\begin{gathered} \frac{\partial^2 P^{n+1}}{\partial x^2} + \frac{\partial^2 P^{n+1}}{\partial y^2} + \alpha\frac{1}{y}\frac{\partial P^{n+1}}{\partial y} = \frac{1+\zeta-\theta}{\theta\Delta\tau}\left(\frac{\partial u^*}{\partial x} + \frac{\partial v^*}{\partial y} + \alpha\frac{v^*}{y}\right) - \frac{1-\theta}{\theta}\left(\frac{\partial^2 P^n}{\partial x^2} + \frac{\partial^2 P^n}{\partial y^2} + \alpha\frac{1}{y}\frac{\partial P^n}{\partial y}\right) \Leftrightarrow \\ \mathrm{div}(\mathrm{grad}\, P)^{n+1} = \frac{1+\zeta-\theta}{\theta\Delta\tau}\mathrm{div}\, \mathbf{c}^* - \frac{1-\theta}{\theta}\mathrm{div}(\mathrm{grad}\, P)^n, \end{gathered} \tag{13}$$

where $\mathbf{c}^* = (u^*, v^*)$ is the tentative velocity vector.

The procedure used is the following. First the time-marching scheme of (10) and (11) is solved to provide the tentative velocity components u^* and v^* and the turbulent variables k and ϵ. Next the Poisson equation is solved using the classical ADI method, which converges fast, and the pressure field is obtained. Finally the velocity components at the new time level are evaluated by correcting the tentative velocity field using (12). For unsteady flows it is essential to fully converge the Poisson equation at each time step in order for the mass conservation to be satisfied.

3.3. *Artificial dissipation terms*

The spatial derivatives in the above system of equations are approximated by three-point, central second-order differencing expressions. Thus the solution of the system of equations (10) requires the inversion of two block tridiagonal systems, one in each direction. On the other hand, the use of central differences leads to the necessity of adding external artificial dissipation terms so that the stability is retained and high-frequency oscillations from the solution are removed. In the present work, only explicitly terms $\mathbf{D}_e$ are used in (11). These terms are a blended second- and fourth-order non-linear model which is widely used in compressible flows[16–19] and was used for the first time in incompressible flows by Pentaris *et al.*[14]

3.4. *Definition of time step*

Although the solution method is implicit, the actual stability of the scheme is not independent of the time step used. In this work, small time steps are used which help the fast convergence of the Poisson equation, although the implicit scheme allows much larger time steps to be used. When a problem with oscillating flow rate is to be simulated, the Navier–Stokes equations must be integrated for as many cycles as are needed to reach a periodic steady state, if such a state exists. In the periodic steady state of period T the solutions at time instants t and $t + T$ must reach a specified convergence criterion, which in the present work is 1×10^{-5}. With the present method this criterion is reached at the second period, because 10,000 time intervals are used per period. Using fewer time intervals per period, more iterations are needed for the convergence of the Poisson equation. In addition, more periods are necessary to reach the above criterion and thus the total computational cost is increased.

When a problem with steady upstream conditions is solved, where the Poisson equation is rapidly converged, the time step must be as large as possible. Then the time step is defined as

$$\mathrm{d}t = \frac{CFL}{1 + \sqrt{J_{\max}}},$$

where $J_{\max}$ is the maximum of all the Jacobians in the computational domain and CFL is the Courant number.

4. BOUNDARY CONDITIONS

Throughout the computations, explicit boundary conditions are used. The Poisson equation is solved under the following pressure boundary conditions. Integrating (13) in the calculation domain E, we get

$$\int_E \operatorname{div}(\operatorname{grad} P^{n+1})\,\mathrm{d}E = \frac{1 + \zeta - \theta}{\theta \Delta\tau} \int_E \operatorname{div} \mathbf{c}^*\,\mathrm{d}E - \frac{1 - \theta}{\theta} \int_E \operatorname{div}(\operatorname{grad} P^n)\,\mathrm{d}E;$$

then, using the Gauss theorem, we obtain

$$\oint_A (\operatorname{grad} P^{n+1}) \cdot \mathbf{n}\, \mathrm{d}A = \frac{1+\zeta-\theta}{\theta \Delta \tau} \oint_A \mathbf{c}^* \cdot \mathbf{n}\, \mathrm{d}A - \frac{1-\theta}{\theta} \oint_A (\operatorname{grad} \mathrm{P}^{\mathrm{n}}) \cdot \mathbf{n}\, \mathrm{dA}, \tag{14}$$

where $\mathbf{n}$ denotes the normal vector to the border A of the domain E. Equation (14) must be used in combination with the Neumann boundary conditions for the pressure. These conditions are applied at each iteration of the ADI method, while the tentative velocity field remains constant in the entire domain. Failure to satisfy (14) results in non-convergent iterative solutions for (13), because a solution does not exist.[20] The compatibility condition (14) is automatically satisfied on staggered grids. Solving the Poisson equations in a full conservative form[14] and using the above-mentioned boundary conditions, full convergence of (13) is obtained although collocated grids are used.

Concerning the other variables, the velocity profiles are specified on the inlet boundary, while the kinetic energy k_{in} is taken to be 0·3% of the turbulence intensity (if experimental data are not available) and the dissipation ϵ_{in} is derived from the relation of the mixing length:

$$k_{\mathrm{in}} = 0{\cdot}003 u_{\mathrm{in}}^2, \qquad \epsilon_{\mathrm{in}} = \frac{C_\mu k_{\mathrm{in}}^{3/2}}{0{\cdot}005 D_{\mathrm{in}}}, \tag{15}$$

where D_{in} is the inlet span.

On the outlet boundary all variables are calculated by extrapolation from the interior. On the symmetry axis the first derivatives of all variables are set equal to zero, except for the v-component of the velocity which itself is set equal to zero. On the solid surface the no-slip condition is applied for the velocity components. The kinetic energy and the dissipation are defined at the first grid point above the solid surface with the use of the wall functions (5).

Finally, as initial conditions, the u-velocity component is set equal to unity, while the v-velocity component and the pressure vanish. The initial data for the turbulence model variables are given by (15). It must be mentioned that the solution is independent of the initial conditions used.

5. RESULTS AND VALIDATION

Some representative results of several test cases are shown in this section. It must be mentioned that all the quantities used are dimensionless. The dimensionless Strouhal and Womersley numbers are defined respectively as

$$Str = \frac{L_{\mathrm{ref}} \omega_{\mathrm{ref}}}{u_{\mathrm{ref}}}, \qquad W = L_{\mathrm{ref}} \sqrt{\left(\frac{\omega_{\mathrm{ref}}}{\nu_{\mathrm{ref}}}\right)} = \sqrt{(Str\, Re)},$$

where ω_{ref} is the reference cyclic frequency. The relation between the physical time $t(s)$ and the dimensionless time t is (note that $t = \tau$)

$$t(s) = \frac{L_{\mathrm{ref}}}{u_{\mathrm{ref}}} \frac{t(s)}{L_{\mathrm{ref}}/u_{\mathrm{ref}}} = \frac{L_{\mathrm{ref}} \omega_{\mathrm{ref}}}{u_{\mathrm{ref}} \omega_{\mathrm{ref}}} \frac{t}{t_{\mathrm{ref}}} = \frac{Str}{\omega_{\mathrm{ref}}} t.$$

Finally it must be noted that all the results have been tested for various grids and are independent of the grid density.

5.1. *One-dimensional oscillatory channel flow*

In order to check the reliability of the present method, it was initially developed for one-dimensional flows and tested on an oscillatory channel flow.[21] In this problem the back pressure of the channel is oscillating according to

$$p_{\mathrm{ex}}(t) = p_0 + p_e \sin(Str\ t).$$

An analytic solution to this problem can only be obtained if the pressure perturbation p, is small compared with the mean back pressure p_0. In this work these parameters are $p_e = 0{\cdot}1$ and $p_0 = 1$. The analytic dimensionless solution for the velocity is

$$u(t) = 1 - \frac{p_e}{1 + Str^2}[\sin(Str\ t) - Str\ \cos(Str\ t) - Str\ e^{-t}]$$

and for the pressure

$$p(x, t) = p_0 + p_e \sin(Str\ t) + (x - 1)\frac{p_e Str}{1 + Str^2}[\cos(Str\ t) + Str\ \sin(Str\ t) + \mathrm{e}^{-t}],$$

where $Str = \omega_{\mathrm{ref}} l / u_0$ is the Strouhal number, chosen to be 10 in this case, based on the mean velocity u_0 and the tube length l.

The above solutions show that the velocity is a function of time only. This is a direct reflection of the incompressible continuity equation in a constant area tube. The pressure fluctuation is a linear function of x that vanishes at $x = 1$ to meet the downstream boundary condition. Some comparisons between the numerical results and the analytic solution are shown in Figure 1. The calculated dimensionless velocity as a function of time (left) and the dimensionless pressure at three longitudinal positions of the tube (right) are compared with the analytic solution. Both numerical results are in excellent agreement with the analytic solution, demonstrating the reliability of the present method for unsteady flows.

5.2. *Two-dimensional periodic flow between parallel plates*

The oscillatory flow between two parallel plates with a span of $2b$ is the second test case we present. The Reynolds number is based on the half-distance b between the two plates and the

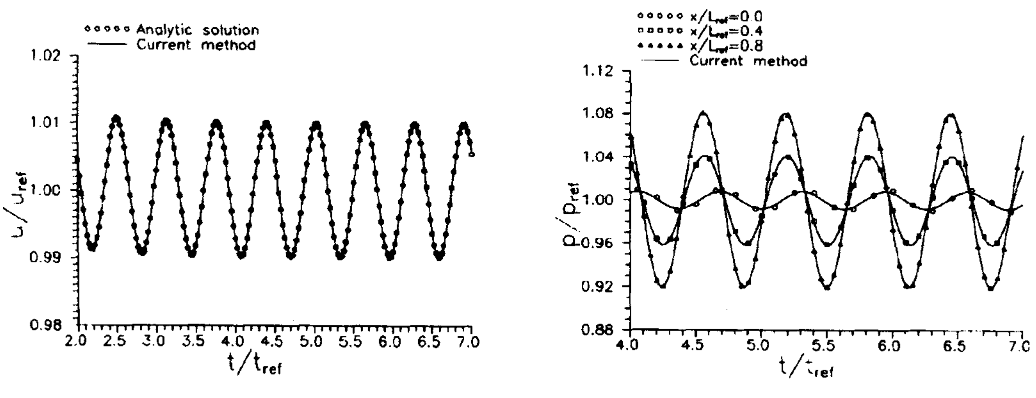

Figure 1. Time evolution of velocity (left) and pressure (right) in one-dimensional channel flow

maximum inflow velocity u_0. Imposing at $x = 0$ the inflow uniform velocity given by

$$u_{\text{in}}(t) = \sin(Str\ t), \qquad v(t) = 0,$$

the analytic solution given by Moore[22] for the developed part of the channel leads to the velocity

$$u_{\text{out}}(t) = \sqrt{\left(\frac{T_1^2 + T_2^2}{I_1^2 + I_2^2}\right)} \sin(Str\ t + \phi_1 - \phi_2)$$

and the pressure gradient

$$\frac{\mathrm{d}p}{\mathrm{d}x}(t) = -\frac{Str}{\sqrt{(I_1^2 + I_2^2)}} \sin(Str\ t - \phi_2).$$

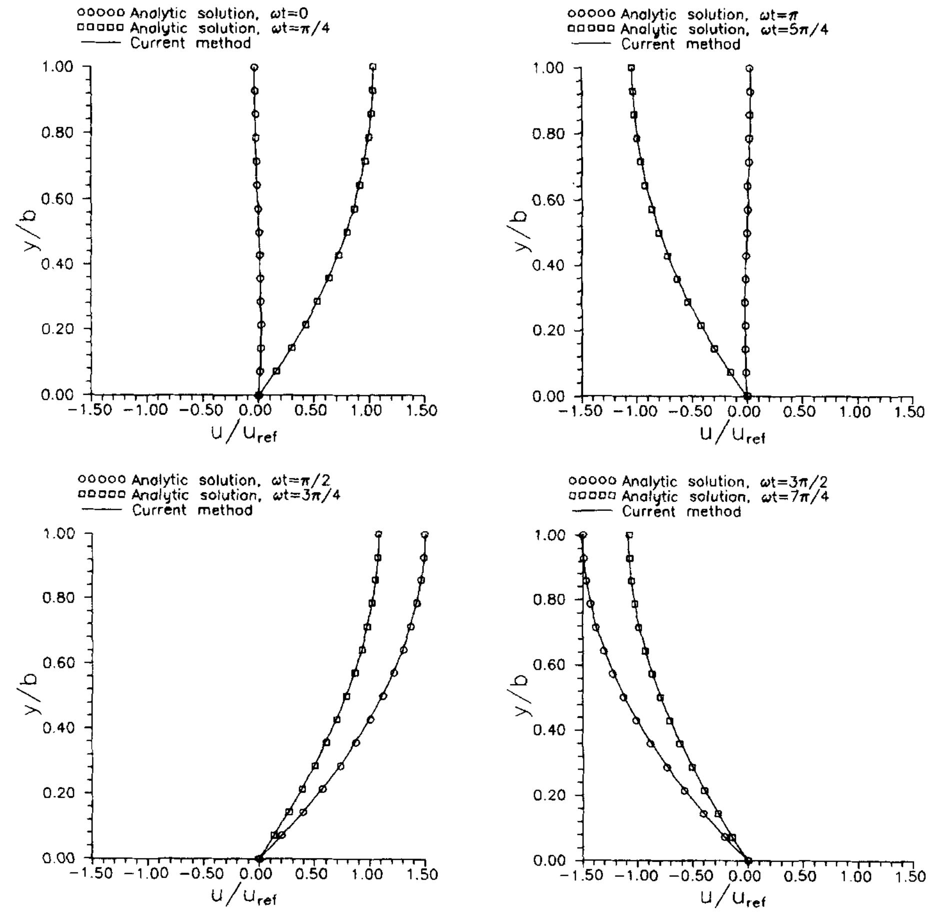

Figure 2. Velocity profiles in developed region of two-dimensional channel for $W = 1$

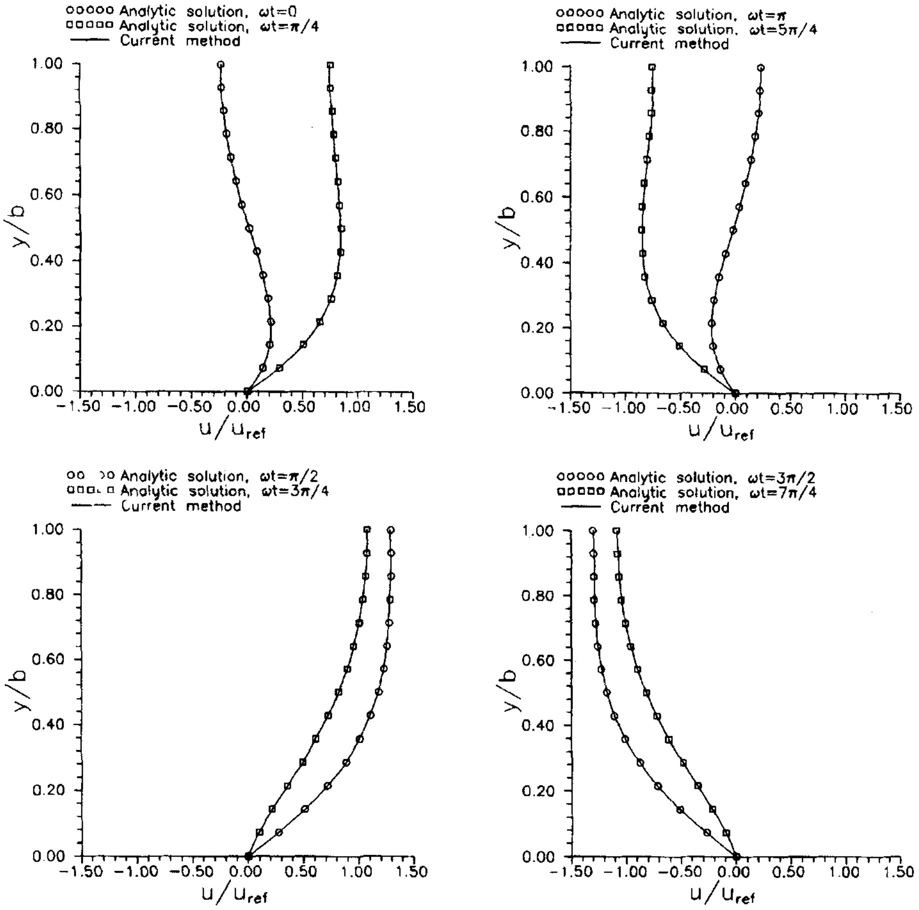

Figure 3. Velocity profiles in developed region of two-dimensional channel for $W = 4$

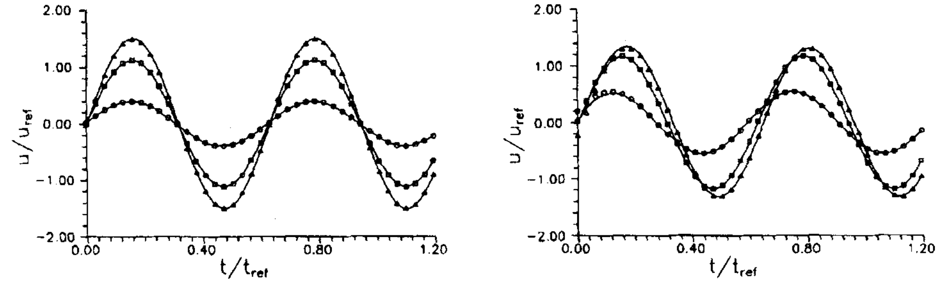

Figure 4. Time evolution of velocity at several positions in developed region of channel for $W = 1$ (left) and $W = 4$ (right)

In the above relations,

$$T_1 = \frac{\cosh(A)\cos(A)\sinh(B)\sin(B) - \sinh(A)\sin(A)\cosh(B)\cos(B)}{\cosh^2(B)\cos^2(B) + \sin^2(B)\sinh^2(B)}$$

$$T_2 = -1 + \frac{\cosh(A)\cos(A)\cosh(B)\cos(B) + \sinh(A)\sin(A)\sinh(B)\sin(B)}{\cosh^2(B)\cos^2(B) + \sin^2(B)\sinh^2(B)}$$

$$I_1 = \frac{1}{2}\int_{-1}^{1} T_1 \mathrm{d}y = \frac{1}{2B}\frac{\sinh(B)\cosh(B) - \sin(B)\cos(B)}{\cosh^2(B)\cos^2(B) + \sin^2(B)\sinh^2(B)},$$

$$I_2 = \frac{1}{2}\int_{-1}^{1} T_2 \, \mathrm{d}y = -1 + \frac{1}{2B}\frac{\sinh(B)\cosh(B) + \sin(B)\cos(B)}{\cosh^2(B)\cos^2(B) + \sin^2(B)\sinh^2(B)},$$

$$\tan(\phi_1) = T_2/T_1, \qquad \tan(\phi_2) = I_2/I_1,$$

where

$$A = \frac{ky}{\sqrt{2}}, \qquad B = \frac{kb}{\sqrt{2}}, \qquad k = \sqrt{\left(\frac{\omega_{\mathrm{ref}}}{\nu_{\mathrm{ref}}}\right)}, \qquad W^2 = (bk)^2 = Re\,Str,$$

$y = 0$ at the midpoint between the two plates, $Str = b\omega/u_0 = 10$ in this case and W is the Womersley number. Two values of this number, $W = 1$ and 4, are used in this paper, with the Reynolds number taking the values 0·1 and 1·6 respectively.

A 75 x 29 grid is used for the current test case, with length $4b$ and height b. The lower boundary ($y = 0$) is a solid wall and the upper one ($y = 1$) is a symmetry axis.

One cycle of the inflow velocity oscillation is split into 10,000 time intervals and the time step obtained is

$$\mathrm{d}t = \frac{2\pi}{Str \times 10\,000} = 2\pi \times 10^{-5}.$$

In Figures 2 and 3 the developed velocity profiles for $W = 1$ and 4 respectively at different physical time instants are presented. As can be seen, the numerical results coincide with the analytic solution. It can be observed that for the smaller Womersley number the profiles keep the form of a developed flow. In Figure 4 the velocity as a function of time is presented at three different distances from the wall. The agreement is excellent between the numerical results and the analytic solution. It can be seen that for $W = 1$ the maximum velocities in each perpendicular position are in phase, which does

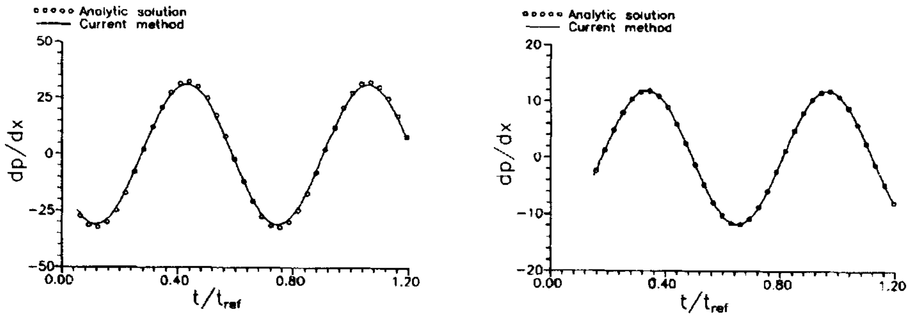

Figure 5. Time evolution of pressure gradient in developed region of channel for $W = 1$ (left) and $W = 4$ (right)

not occur for $W = 4$. In addition, it is clear that the unsteady motion is predicted well after one-fourth of the first period, which is one reason for the use of small time steps. The same conclusions are derived from Figure 5, where the pressure gradients in the developed part as a function of time are presented for both Womersley numbers.

5.3. Axisymmetry periodic channel flow

The third test case under consideration is the periodic flow in a circular tube, extensively presented and analysed by many researchers.[23–26] In the present paper the Reynolds number, based on the radius α of the tube and the maximum inflow velocity u_0, is considered to be equal to 0·1 in order to approximate the Stokes flow. At $x = 0$ the imposed velocity profile is[26]

$$u(t) = u(y)\ \cos(Str\ t), \qquad v(t) = 0.$$

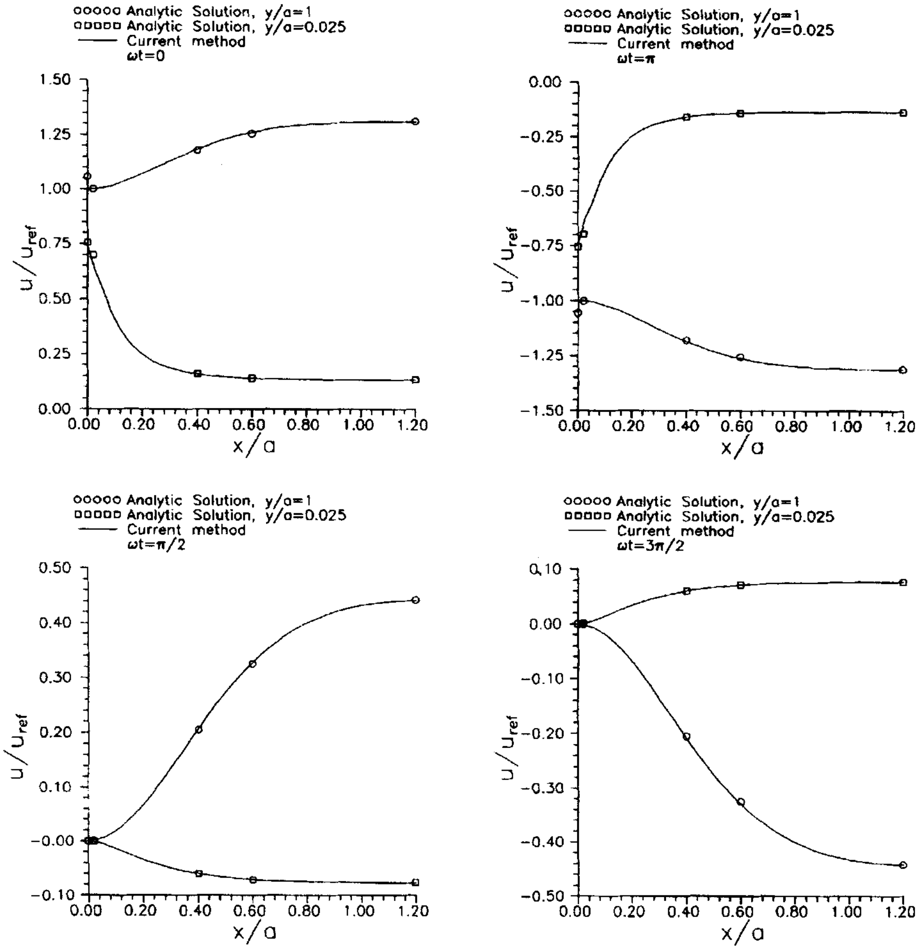

Figure 6. Longitudinal velocity component along circular tube for one cycle of flow

Since many problems of practical interest deal with entrance flow difficulties, in the present study we set

$$u(y) = \begin{cases} 1 - (0{\cdot}05 - y)^2/0{\cdot}05^2 & \text{when } 0 \leqslant y \leqslant 0{\cdot}05, \\ 1 & \text{when } 0{\cdot}05 < y \leqslant 1, \end{cases}$$

so that the axial velocity at the entrance of the tube is uniform except near the wall ($y = 0$), where it parabolically approaches zero in a small layer region.

For the present case we select the typical Womersley number $W = \alpha\sqrt{(\omega_{\text{ref}}/\nu_{\text{ref}})} = \sqrt{30}$ and the Strouhal number becomes $Str = \alpha\omega_{\text{ref}}/u_{\text{ref}} = 300$. The time step used is $dt = 2{\cdot}094 \times 10^{-6}$.

A 45×40 grid is used, with length $1{\cdot}2\alpha$ and height α. The lower boundary ($y = 0$) is a solid wall and the upper one ($y = 1$) is a symmetry axis.

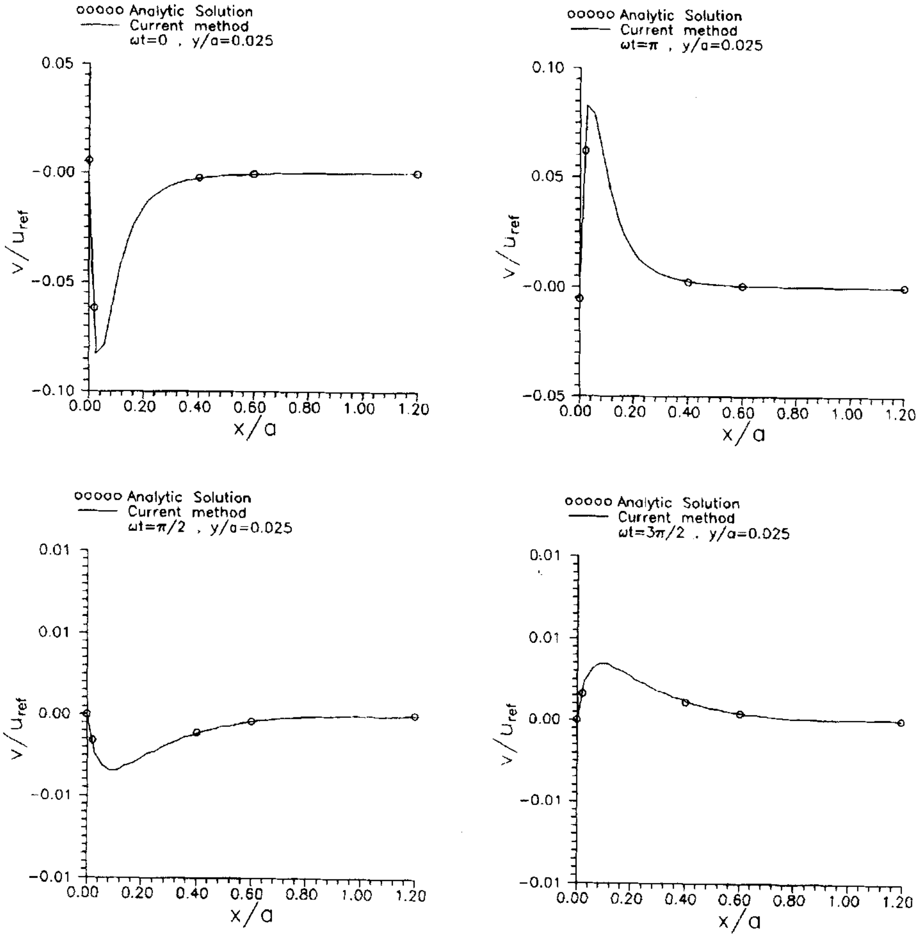

Figure 7. Radial velocity component along circular tube for one cycle of flow

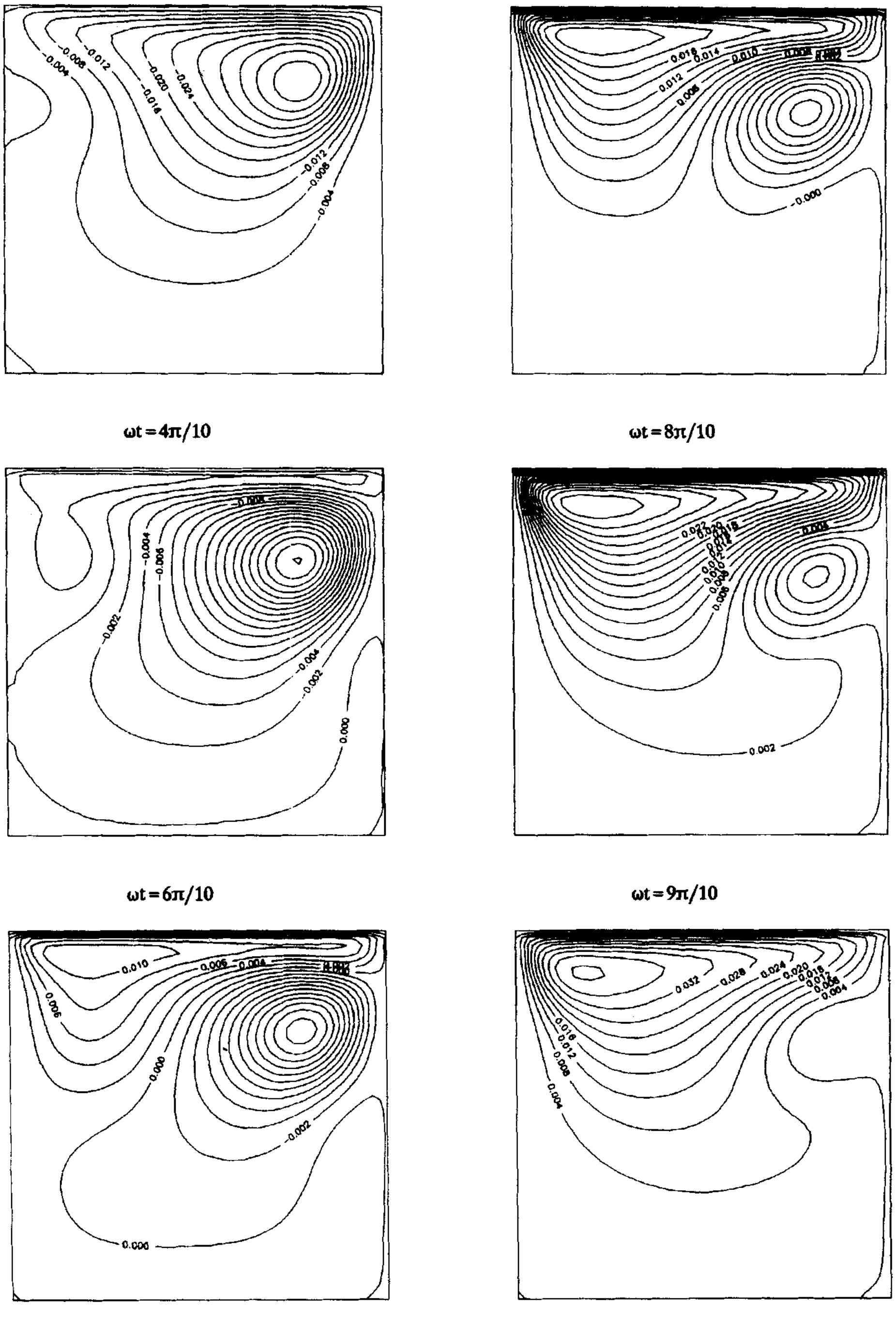

$\omega t = 4\pi/10$ $\omega t = 8\pi/10$

$\omega t = 6\pi/10$ $\omega t = 9\pi/10$

$\omega t = 7\pi/10$ $\omega t = \pi$

Figure 8(a). Streamline contours for one complete cycle inside cavity

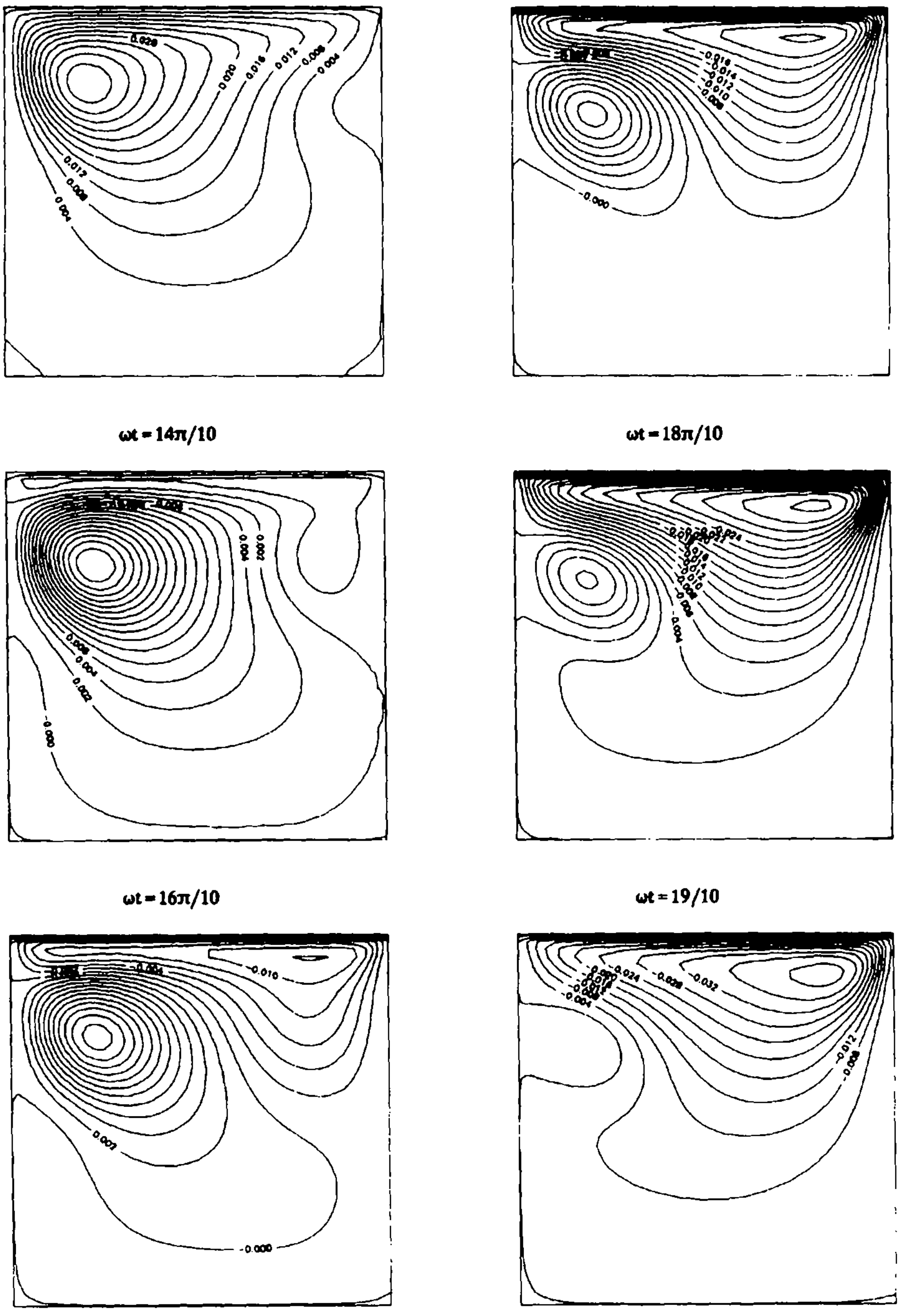

$\omega t = 14\pi/10$

$\omega t = 18\pi/10$

$\omega t = 16\pi/10$

$\omega t = 19/10$

$\omega t = 17\pi/10$

$\omega t = 2\pi$

Figure 8(b). Streamline contours for one complete cycle inside cavity

The solutions for the velocity components and the excess extrance pressure are expressed in the form

$$u(x, y, t) = A_u \cos(Str\, t + \theta_u), \qquad v(x, y, t) = A_v \cos(Str\, t + \theta_v),$$
$$p(x, y, t) = A_p \cos(Str\, t + \theta_p),$$

where A_u, A_v and A_p represent amplitudes and θ_u, θ_v and θ_p phases of the solutions. Note that each of the above amplitudes and phases of the solution is dependent upon both the co-ordinates x and y. Solutions for the above relations are given by Goldberg *et al.*[26] in their Table I (note that their product $W\,T$ is equivalent to our $Str\ t$).

In Figures 6 and 7, comparisons between the semianalytic solution[26] and the numerical results provided by the current method are given for the two velocity components at four instants of physical time. The axial velocity component u is presented along the centreline ($y = 1$) and near the wall ($y = 0{\cdot}025$), as a function of the distance from the entrance. The radial velocity component v is shown at $y = 0.025$. The agreement of the numerical results with the semianalytic solution is very good at all time instants. Discrepancies that occur in the centreline velocity at $\omega t = 0$ and $\omega t = \pi$ at $x = 0$ are due to the semianalytic solution.[26]

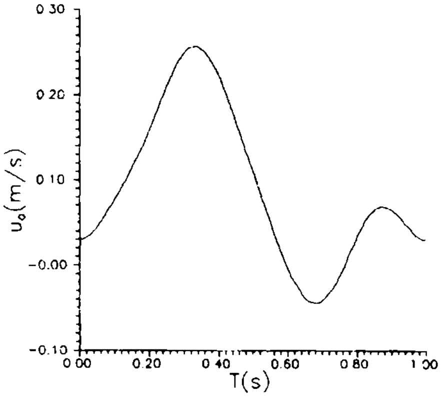

Figure 9. Pulse velocity as a function of time

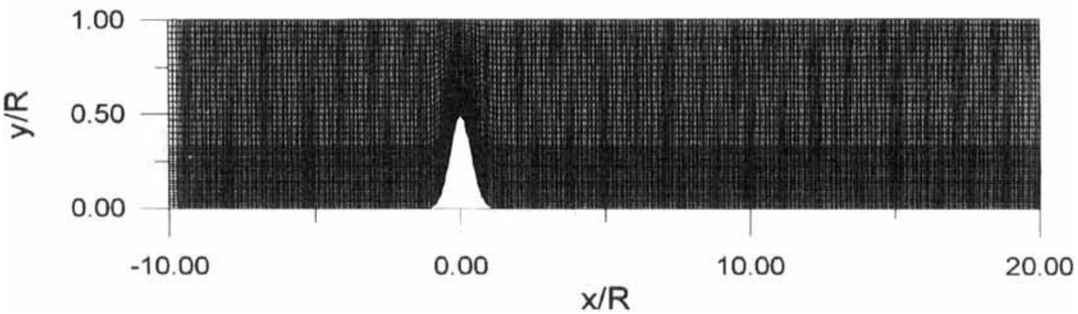

Figure 10. Geometry of stenosis and 419 × 41 grid

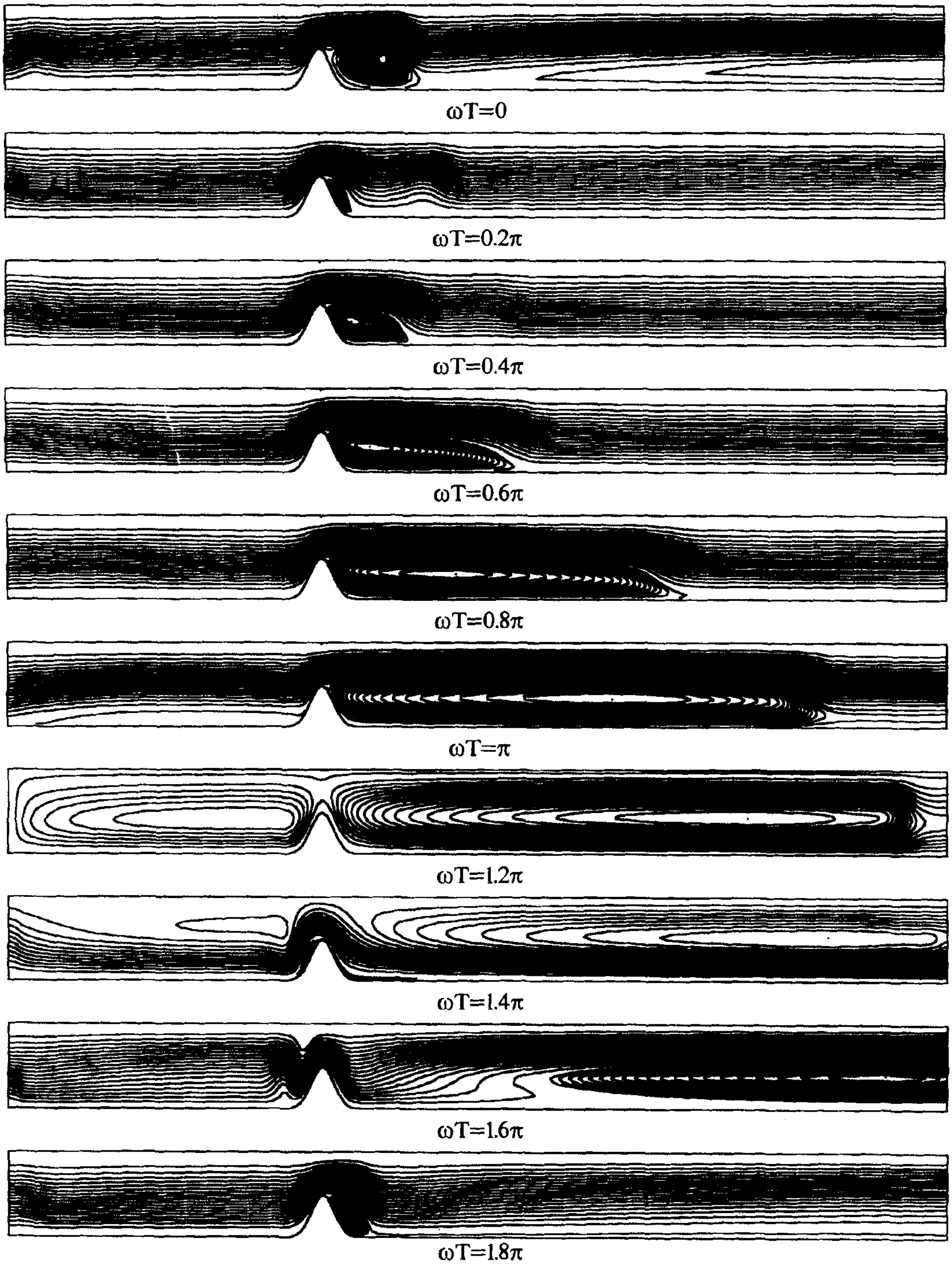

Figure 11. Streamline contours for one complete cycle of flow in stenosis

5.4. *Oscillatory flow inside a square cavity*

The fourth computational test we present is a flow in a driven cavity with a time-periodic lid velocity. The Reynolds number, based upon the maximum lid velocity u_0 and the length of the cavity side, is equal to 400. The oscillating lid velocity is given as[27]

$$u(t) = \cos(Str\ t), \qquad v(t) = 0.$$

The Strouhal number is equal to unity and the time step obtained is $dt = 2\pi \times 10^{-4}$. A uniform 80×80 grid is used.

In Figures 8(a) and 8(b) the streamline contours for the periodic steady solution are presented. Each plot corresponds, in order to the sequence of physical time $\omega t = 2\pi\gamma/40$, where $\gamma = 8$, 12, 14, 16, 18, 20, 28, 32, 34, 36, 38 and 40. These time instants are used in order for our results to be comparable with the numerical results provided by Soh and Goodrich[27] (their Figure 9). A symmetry consideration leads us to expect that flows at time instants t and $t + T/2$ are mirror images of each other about $x = 0{\cdot}5$ and the streamline contours clearly indicate the symmetry between Figures 8(a) and 8(b).

5.5. *Pulsatile flow through an axisymmetric stenosis*

The unsteady flow through an axisymmetric stenosis is the next case we present. This kind of flow is of great interest because of its relation to the human vessels and the possibility of diagnosing the stenosis in its earlier stages. In this work we deal with the physiological pulsatile flow. The stenosis is considered as a single smooth constriction in a long straight circular tube and its geometry is given as[28]

$$y(x) = 1 - 0{\cdot}5\ \exp(-4x^2),$$

where x and y are normalized by the unconstricted tube radius R. The degree of the stenosis is 70%.

The Reynolds number, based upon the radius $R = 0{\cdot}005$ m and twice the peak spatial average velocity $u_{\max} = 0{\cdot}1348\ \mathrm{m\,s^{-1}}$ at the inlet section, is $Re = 2u_{\max}R/\nu_{\mathrm{ref}} = 337$. The Womersley number used is 6·27. The time step used is $dt = 0{\cdot}0054$. At the entrance a time-dependent parabolic velocity profile is imposed,[29]

$$u(t) = \frac{u_0(t)}{2u_{\max}}(1 - y^2), \qquad v(t) = 0,$$

where $u_0(t)$ is the pulse velocity in metres per second, shown in Figure 9.

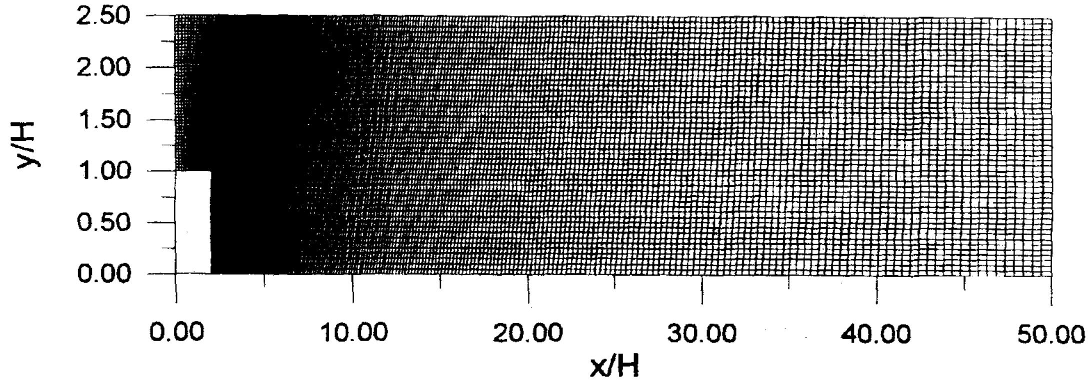

Figure 12. Geometry of step and 250 × 50 grid

For the present test case a 419 × 41 grid is used as shown in Figure 10. The lower boundary ($y = 0$) is a solid wall and the upper one ($y = 1$) is a symmetry axis.

The instantaneous streamlines during one cycle of physiological pulsatile flow are shown in Figure 11. Our results are at the same physical time instants as the numerical results presented by Tu *et al.*[29] (their Figure 9). The comparison between the two numerical methods shows very good agreement. At $\omega T = 0{\cdot}2\pi$ the streamline runs smoothly through the stenosis and a small vortex develops. As the flow accelerates during systale, the vortex becomes bigger and it continues to grow even after the flow decelerates after $\omega T = 0{\cdot}6\pi$. At $\omega T = \pi$ the flow reverses direction near the wall, upstream of the stenosis, and another vortex develops in this region. When the flow at the entrance section starts to reverse direction at about $\omega T = 1{\cdot}2\pi$, both vortices grow in size, detach from the stenosis and fill most of the circular tube. The influence of the reversed flow downstream of the stenosis can be seen here. The vortex is forced towards the axis by this reversed flow near the wall. At $\omega T = 1{\cdot}6\pi$ the flow reverses direction for a second time and accelerates during diastole, the upstream vortex is diffused and the downstream vortex is carried out by the flow.[28] At $\omega T = 1{\cdot}8\pi$, when the flow decelerates, a small vortex develops again and it becomes bigger at $\omega T = 0$. After that time the flow smooths out and the cycle starts again with the systole.

5.6. Unsteady flow behind a backward-facing step

For many years, turbulence in fluids has been the subject of uninterrupted efforts aimed at unveiling the mystery of its dynamics. An important idea which has recently emerged is the concept of coherent vortices, corresponding to local vorticity concentration of lifetime much longer than its turnover time. These coherent vortices play an important role in numerous technological applications and its is necessary to understand the dynamics of these organized motions so as to mechanically control their production or suppression. In high-Reynolds-number mixing layers, Kelvin–Helmholtz coherent vortices were identified by Brown and Roshko.[30] Recent numerical studies deal with separated flows in various geometries. In the present paper a numerical investigation of the coherent vortices in turbulence behind a backward-facing[31] step is presented.

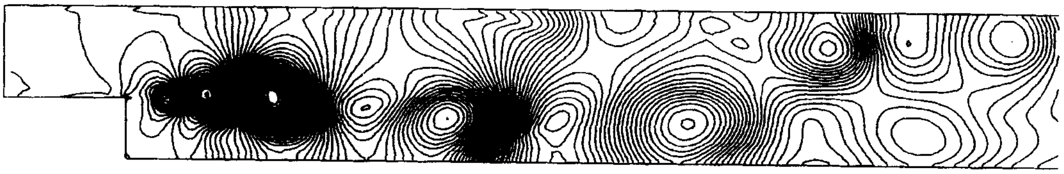

Figure 13. Pressure contours for unsteady flow in backward-facing step

Figure 14. Vorticity contours for unsteady flow in backward-facing step

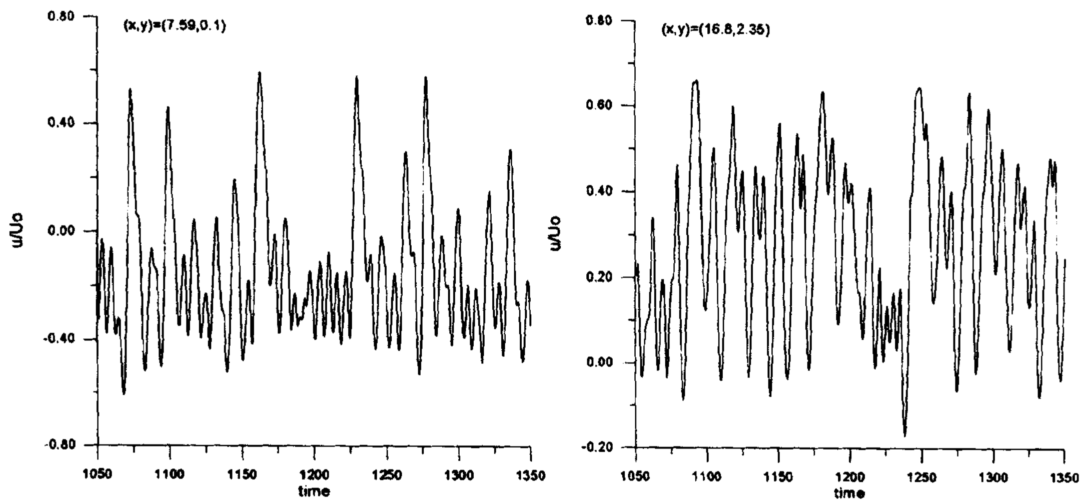

Figure 15. Time evolution of longitudinal velocity at $x/H = 7{\cdot}59, y/H = 0{\cdot}1$ (left) and $x/H = 16{\cdot}8, y/H = 2{\cdot}35$ (right) for unsteady flow in backward-facing step

The ratio of the channel height W to the step height H is $W/H = 2{\cdot}5$. The geometry and the inflow velocity profile $U(y)$ are the same as in the experiments of Eaton and Johnston.[32] Two grids of dimensions 150 × 40 and 250 × 50 were used. The denser one is shown in Figure 12. The total length of the channel is 50 step heights. Both the lower and upper boundaries are solid surfaces. The Reynolds number, based upon the step height H and the maximum inflow velocity U_0, is 38,000. The time step used is $dt = 0{\cdot}0075$.

In the first run the original $k - \epsilon$ model was used. The flow that occurred was steady and the recirculation length was $7{\cdot}1H$. The main reason that a steady flow was predicted is the overestimate of the turbulent kinematic viscosity, which indirectly reduces the Reynolds number. Thus a second run was performed using the relation

$$\nu_t = C_\mu f_\mu \frac{k^2}{\epsilon}, \qquad f_\mu = f_o + (1 - f_o)\{1 - \exp[-(y^+ - y_o^+)/A^+]\}^2,$$

proposed by Miner *et al.*,[33] where $f_0 = 0{\cdot}04$, $y_0^+ = 8$ and $A^+ = 26$. The above relation is used in order to reduce the turbulence viscosity in the near-wall region ($y^+ < 120$), where $f_\mu < 1$.

The flow now becomes unsteady. The pressure contours are shown in Figure 13 and the vorticity contours in Figure 14. The presence of a mixing layer behind the step is shown. The recirculation length is overestimated as $8{\cdot}1H$, compared with the experimental result of $7{\cdot}8H$ (temporal mean) and the other numerical result of Silveira Neto *et al.*[31] of $6{\cdot}8H$. The eddies which impinge on the lower wall and are transported downstream are shed with a frequency f that corresponds to a Strouhal number $Str = fH/U_0 \approx 0{\cdot}068$ for the denser grid and $0{\cdot}072$ for the coarse one. This is in good agreement with the experimental value, $Str \approx 0{\cdot}07$. In Figure 15 the temporal evolution of the longitudinal velocity component at $x/H = 7{\cdot}59, y/H = 0{\cdot}1$ and $x/H = 16{\cdot}8, y/H = 2{\cdot}35$ is shown. In Figure 16 the time-mean velocity profiles at two different positions are shown in comparison with the experimental data of Eaton and Johnson[32] and the numerical results of Silveira Neto *et al.*[31] The agreement with the experimental data is very good. These profiles were integrated in about 42,000 time steps and were almost identical for both grids used.

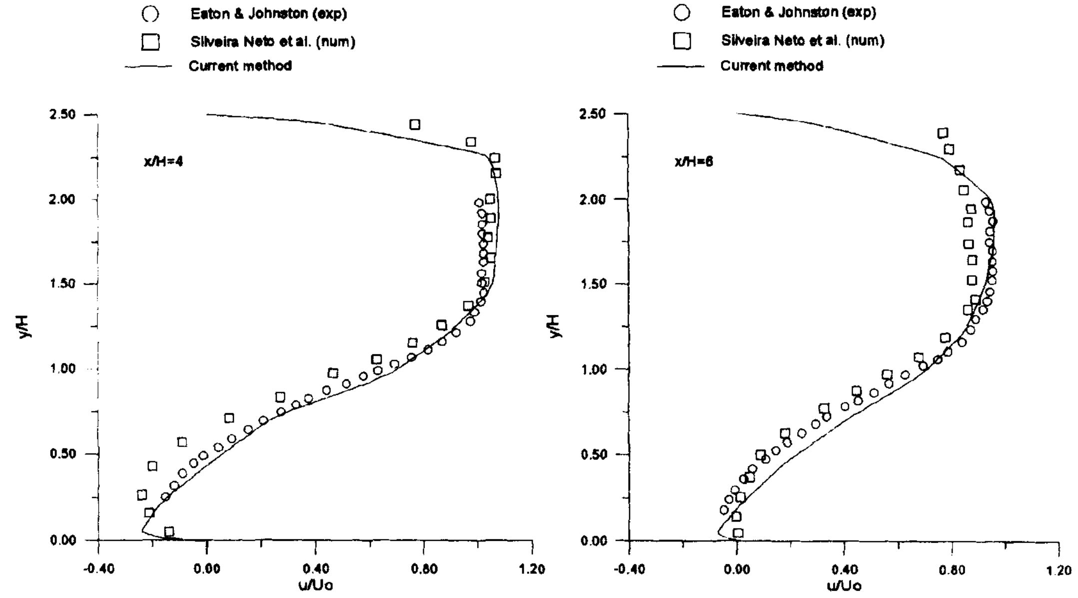

Figure 16. Longitudinal velocity profiles versus experimental data and other numerical results

An interesting phenomenon is the separation of the boundary layer from the upper wall; it generates a second street of coherent vortices which are transported towards the outlet of the channel with a Strouhal number $Str \approx 0{\cdot}068$. This phenomenon has also been observed in experiments performed by Armaly *et al.*[34]

6. CONCLUSIONS

An implicit projection method for the solution of the unsteady Navier–Stokes equations on collocated grids is presented in this paper. The computational method is based on the approximate factorization technique and the incompressibility constraint is satisfied by a Poisson equation. Extended comparison with analytic solutions, experimental data and numerical results provided by other researchers lead to the conclusion that the present methodology is a reliable tool for solving a large range of unsteady problems.

REFERENCES

1. A. J. Chorin, 'Numerical solution of the Navier–Stokes equations', *Math. Comput.*, **22**, 745–762 (1968).
2. R. Temam, 'Sur l'approximation de la solution des equations de Navier–Stokes par la methode des pas fractionnaires (II)', *Arch. Rat. Mech. Anal.*, **32**, 377–385 (1969).
3. M. Fortin, R. Peyert and T. Temam, 'Resolution numerique des equations de Navier–Stokes pour un fluide incompressible', *J. Méc*, **10**, 357–390 (1971).
4. R. Temam, *Navier–Stokes Equations*, North-Holland, Amsterdam, 1979.
5. R. M. Beam and R. F. Warming, 'An implicit factored scheme for the compressible Navier–Stokes equations', *AIAA J.*, **16**, 393–402 (1978).
6. V. Michelassi and C. Benocci, 'Prediction of incompressible flow separation with the approximate factorization technique', *Int. j. numer. methods fluids*, **7**, 1383–1403 (1987).
7. M. L. Mansour and A. Hamed, 'Implicit solution of the incompressible Navier–Stokes equations on a non-staggered grid', *J. Comput. Phys.*, **86**, 147–167 (1990).

8. B. E. Launder and D. B. Spalding, 'The numerical computation of turbulent flows', *Comput. Methods Appl. Mech. Eng.*, **3**, 269–289 (1974).
9. Q. Zhong and M. D. Olson, 'Periodic solution of turbulent oscillating channel flows', *Int. j. numer. methods fluids*, **14**, 443–457 (1992).
10. J. Cousteix, A. Desopper and R. Houdeville, 'Structure and development of a turbulent boundary layer in an oscillatory external flow', in *Turbulent Shear Flows I*, Springer, Berlin, 1977, pp. 154–171.
11. G. Binder and J. L. Kueny, 'Measurements of the periodic velocity oscillations near the wall in unsteady turbulent channel flow', in *Unsteady Turbulent Shear Flow, IUTAM Symp.*, Springer, Berlin, 1981, pp. 100–108.
12. S. Tsangaris, M. P. Thomadakis and A. Pentaris, 'Numerical investigation of axisymmetric compressible viscous flow', *Proc. 1st Eur. Computational Fluid Dynamics, Conf.*, Brussels, 1992, pp. 835–842.
13. H. I. Anderson and R. Kristoffersen, 'Numerical simulation of unsteady viscous flow', *Arch. Mech.*, **41**, 207–223 (1989).
14. A Pentaris, K. Nikolados and S. Tsangaris, 'Development of projection and artificial compressibility methodologies using the approximate factorization technique', *Int. j. numer. methods fluids*, **19**, 1013–1038 (1994).
15. V. Michelassi and C. Benocci, 'Efficient solution of turbulent incompressible separated flows', *Proc. 8th GAMM Conf. on Numerical Methods in Fluid Mechanics*, 1989, Vieweg, Braunschweig, 1990, pp. 373–390.
16. A. Jameson, W. Schmidt and E. Turkel, 'Numerical solutions of the Euler equations by finite volume methods using Runge–Kutta time-stepping schemes', *AIAA Paper 81-1259*, 1981.
17. T. H. Pulliam, 'Artificial dissipation models for the Euler equations', *AIAA J.*, **24**, 1931–1940 (1986).
18. M. P. Thomadakis and S. Tsangaris, 'Improved artificial dissipation schemes for the Euler equations', *Int. j. numer. methods fluids*, **14**, 1391–1405 (1992).
19. F. Dejean, C. Vassilopoulos, G. Simandirakis, K. C. Giannakoglou and K. D. Papailou, 'Analysis of 2-D transonic turbomachinery flows using an explicit low-Reynolds $k - \epsilon$ Navier–Stokes solver', *Proc. 39th ASME Int. Gas Turbine and Aeroengine Congr. Expos.*, The Hague, June 1994.
20. F. Sotiropoulos and S. Abdallah, 'Coupled fully implicit solution procedure for the steady incompressible Navier–Stokes equations', *J. Comput. Phys.*, **87**, 328–348 (1990).
21. C. L. Merkle and M. Athavale, 'Time-accurate unsteady incompressible flow algorithms based on artificial compressibility', *AIAA Paper 87-1137*, 1987.
22. F. K. Moore, *Theory of Laminar Flows*, Princeton University Press, Princeton, NJ, 1964.
23. H. B. Atabek and C. C. Chang, 'Oscillatory flow near the entry of a circular tube', *Z. Angew. Math. Phys.*, **12**, 185–201 (1961).
24. C. C. Chang and H. B. Atabek, 'The inlet length for oscillatory flow and its effects on the determination of the rate of flow in arteries', *Phys. Med. Biol.*, **6**, 303–317 (1961).
25. H. B. Atabek, C. C. Chang and L. M. Fingerson, 'Measurement of laminar oscillatory flow in the inlet length of a circular tube', *Phys. Med. Biol.*, **9**, 219–227 (1964).
26. I. S. Goldberg, G. F. Carey, R. McLay and L. Phinney, 'Periodic viscous flow: a bench-mark problem', *Int. j. numer. methods fluids*, **11**, 87–97 (1990).
27. W. Y. Soh and J. W. Goodrich, 'Unsteady solution of incompressible Navier–Stokes equations', *J. Comput. Phys.*, **79**, 113–134 (1988).
28. M. Siouffi, R. Pelissier, D. Farahifar and R. Rieu, 'The effect of unsteadiness on the flow through stenoses and bifurcations', *J. Biomech.*, **17**, 299–315 (1984).
29. C. Tu, M. Deville, L. Dheur and L. Vanderschuren, 'Finite element simulation of pulsatile flow through arterial stenosis', *J. Biomech.*, **25**, 1141–1152 (1992).
30. G. L. Brown and A. Roshko, 'On the density effects and large structure in two-dimensional mixing layers', *J. Fluid Mech.*, **64**, 775–816 (1974).
31. A. Silveira Neto, D. Grand, O. Metais and M. Lesiuer, 'A numerical investigation of the coherent vortices in turbulence behind a backward-facing step', *J. Fluid Mech.*, **256**, 1–25 (1993).
32. J. K. Eaton and J. P. Johnston, 'Turbulent flow re-attachment: an experimental study of the flow and structure behind a backward-facing step', *Stanford University Rep. Md-39*, 1980.
33. E. W. Miner, T. F. Swean, R. A. Handler and R. I. Leighton, 'Examination of wall damping for the $k - \epsilon$ turbulence model using direct simulations of turbulent channel flow', *Int. j. numer. methods fluids*, **12**, 609–624 (1991).
34. B. F. Armaly, F. Durst, J. C. Pereira and B. Schonung, 'Experimental and theoretical investigation of backward-facing step flow', *J. Fluid Mech.*, **127**, 423–496 (1983).